Clays Clay Miner., Vol. 70, No. 1:84–105, 2022
https://doi.org/10.1007/s42860-022-00174-9

ORIGINAL PAPER

A FIB-SEM Study of Illite Morphology in Aeolian Rotliegend Sandstones: Implications for Understanding the Petrophysical Properties of Reservoir Rocks

Markus Peltz · Arne Jacob · Georg H. Grathoff · Frieder Enzmann · Michael Kersten · Laurence N. Warr

Accepted: 13 January 2022

Abstract Diagenetic illite growth in porous sandstones leads to significant modifications of the initial pore system which result in tight reservoirs. Understanding and quantifying these changes provides insight into the porosity-permeability history of the reservoir and improves predictions on petrophysical behavior. To characterize the various stages of diagenetic alteration, a focused ion beam – scanning electron microscopy (FIB-SEM) study was undertaken on aeolian sandstones from the Bebertal outcrop of the Parchim Formation (Early Permian Upper Rotliegend group). Based on 3D microscopic reconstructions, three different textural types of illite crystals occur, common to many tight Rotliegend sandstones, namely (1) feldspar grain alterations and associated illite meshworks, (2) tangential grain coats, and (3) pore-filling laths and fibers. Reaction textures, pore structure quantifications, and numerical simulations of fluid transport have revealed that different generations of nano-porosity are connected to the diagenetic alteration of feldspars and the authigenic growth of pore-filling illites. The latter leads to the formation of microstructures that range from authigenic compact tangential grain coatings to highly porous, pore-filling structures. K-feldspar replacement and initial grain coatings of illite are composed primarily of disordered $1M_d$ illite whereas the epitaxially grown illite lath- and fiber-shaped crystals occurring as pore-filling structures are of the *trans*-vacant $1M_{tv}$ polytype. Although all analyzed 3D structures offer connected pathways, the largest reduction in sandstone permeability occurred during the initial formation of the tangential illite coatings that sealed altered feldspars and the subsequent growth of pore-filling laths and fibrous illites. Analyses of both illite pore-size and crystallite-size distributions indicate that crystal growth occurred by a continuous nucleation and growth mechanism probably controlled by the multiple influx of potassium-rich fluids during late Triassic and Jurassic times. The detailed insight into the textural varieties of illite crystal growth and its calculated permeabilities provides important constraints for understanding the complexities of fluid-flow in tight reservoir sandstones.

Keywords Illite morphology · Focused ion beam polishing · Computational fluid dynamic simulations · Pore-size distributions · Clay mineral diagenesis

M. Peltz (✉) · G. H. Grathoff · L. N. Warr
Institute of Geography and Geology, University of Greifswald, F.-L.-Jahn-Str. 17a, 17489 Greifswald, Germany
e-mail: markus.peltz@uni-greifswald.de

A. Jacob · F. Enzmann · M. Kersten
Institute of Geosciences, Johannes Gutenberg-University, J.-J. Becherweg 21, 55099 Mainz, Germany

Introduction

Aeolian sandstones from the Early Permian Upper Rotliegend group constitute important geological reservoirs for natural gas in the Southern Permian Basin (SPB) and, once exploited, present potential sites for future gas storage. To assess reliably the storage potential of these rocks and to determine their petrophysical

properties (e.g. porosity and permeability), detailed knowledge of the pore-filling diagenetic-mineral inventory and its associated pore-space characteristics is required. These properties were initially controlled by the depositional environment and then altered during multiple stages of burial diagenesis and subsequent regional-scale fluid-flow events (Darby et al., 1997; Bjørlykke, 2014).

Claymineral paragenesis represents an important indicator of reservoir quality. Whereas the presence of chlorite rims is often related to high permeability and the preservation of porosity (Morad et al., 2010), the occurrence of smectite, mixed-layer illite-smectite, or pure illite generally reflects more restrictive changes to the initial pore system such as a reduction in flow paths within sandstones. Illites and illitic minerals found in reservoir sandstones from the North Sea area and the North German Basin have been studied extensively in the past (Glennie et al., 1978; Hancock, 1978; Seemann, 1982; Ziegler, 2006; Gaupp & Okkerman, 2011; Weibel et al., 2020). Based on their origin, they can be divided into (1) detrital illite/muscovite, (2) illitic minerals that form by solid-state transformations of different precursor phases, and (3) authigenic illite crystals grown in the pore space.

Tangential grain coatings of illite are observed frequently in sandstones. They are described commonly as composed initially of either detrital illite/muscovite or amorphous to smectitic precursor phases (Griffiths et al., 2018) that infiltrated during deposition by aeolian transport or during early diagenesis by colloidal suspensions (Ziegler, 2006; Tang et al., 2018). Illites of detrital origin in these environments are usually of the $2M_1$ polytype and form thicker crystallites compared to other types of illite (Aldega & Eberl, 2005). With increasing burial, and temperatures >70°C (Merriman & Kemp, 1996), a well studied diagenetic illitization sequence starts with smectites transforming progressively through different stages of illite-smectite interstratifications to form illite with minor amounts (<5%) of interstratified smectite (Gharrabi, 1998). These illites are also referred to as poorly crystalline illites (Meunier & Velde, 2004) or $1M_d$ illite (Aldega & Eberl, 2005). Small et al. (1992) synthesized similar illite coatings from solution at various temperatures and with various morphologies that contain the ordered $1M$ as well as the $1M_d$ polytypes. None of the coatings observed showed a strictly tangential structure thought to indicate allochthonous infiltrated particles, however (Wilson, 1992).

The formation of late diagenetic authigenic illite is well documented in Mesozoic and Cenozoic porous sandstones across central and northwest Europe and has been related to basin-wide hydrothermal fluid-flow events linked to the opening of the Atlantic ocean (Zwingmann et al., 1998; Wilkinson et al., 2014). In contrast to burial-related illitization, these illites typically neocrystallized directly from formation fluids that were super-saturated in potassium. The crystal morphology of these precipitates has long been recognized and ranges from platy through lath-shaped to fibrous particles (Wilson & Pittman, 1977). K-feldspars, kaolinite, detrital mica grains, or grain-coating illites are known to serve as a substrate for subsequent illite growth, which commonly produces the trans-vacant (tv) $1M$ polytype variety with fibrous and lath-shaped crystal habits (Meunier & Velde, 2004; Lander & Bonnell, 2010). In contrast, the cis-vacant (cis) $1M$ polytype variety is considered to form at higher temperatures and is often associated with greater crystallinity and platy crystal shapes (Lanson et al., 2002). Lath- to fiber-shaped particles are interpreted to grow more rapidly in potassium-enriched fluids (Wilkinson et al., 2014), which is in accordance with the diverse crystal shapes synthesized in the laboratory under varying chemical conditions at a fixed temperature (Bauer et al., 2000). In terms of the petrophysical properties of the reservoir rock, the occurrence of fibrous illite is known as the main cause of permeability reduction in reservoir sandstones (Weibel et al., 2020). The occurrence of multiple generations of illite in porous rocks has also provided an ideal opportunity to determine the K-Ar ages of these hydrothermal mineralization events across Europe, which has revealed numerous fluid-flow events spanning a period of 200 million years that affected both sedimentary basins and underlying basement rocks (Zwingmann et al., 1998; Schleicher et al., 2006).

Although the mechanism of crystallization and the relationships between fluid composition and crystal growth are now well studied, the interaction between the growth of illite crystals in the pores of reservoir sandstones and the subsequent changes in pore space and fluid flow behavior is quantitatively less well understood. Desbois et al. (2016) analyzed illite-related microstructures in a German Rotliegend sandstone by broad ion beam polishing (BIB), focused ion beam polishing (FIB), and scanning electron microscopy (SEM), and proposed a fundamental building block model for quantifying the influence of nanoporous

structures on fluid flow. Currently, most conventional rock models used for computational fluid dynamic simulations differentiate between the void pore space and the solid mineral matrix at the μm-scale only, while the proposed digital rock model of Desbois et al. (2016) includes mineral-specific properties derived from nm-scale observations. Jacob et al. (2021) adapted this idea and developed a conceptual fluid-flow model to calculate flow parameters for illite-dominated sandstones based on FIB-SEM and micro-CT-generated 3D pore-space reconstructions, although the various nano-porous textural groups common to these rocks were not considered.

To address the influence of microtextural variability, the purpose of the present study was to combine XRD-based polytype quantifications with SEM and site-specific FIB-SEM studies to understand better the relationship between the different types of illite crystal growth features and dynamic fluid flow-related changes that occurred in the pore space of a well-studied Rotliegend sandstone sample block from the Bebertal outcrop, northern Germany. The objectives were (1) to determine the reaction textures and petrophysical properties of the selected FIB-SEM domains relevant to porosity, permeability, and simulated fluid flow, and (2) to place these results in the context of the rock's diagenetic history marked by initial burial and Triassic and Jurassic fluid-flow events that spanned at least 50 million years of geological time.

Material

The ~265 Ma old Upper Rotliegend sandstones from the Parchim Formation (Havel sub-group) present an ideal natural analogue for deeply buried gas-bearing reservoirs (Menning et al., 2006; Gaupp & Okkerman, 2011). They are located at the southern margin of the Northern German Basin (NGB), which formed as a sub-basin of the Southern Permian Basin (SPB). The Bebertal outcrop exposed in Schwentesius quarry (N 52.2564084°; E 11.3361657°) represents the northernmost exposure of this formation and is located close to Magdeburg, Germany. The upper 12 m of the quarry is composed of aeolian cross-bedded and laminated sandstone with thin layers of clay-rich fluvial sheet-flow deposits (Fischer et al., 2012). The main lithology consists of moderate- to well-sorted, medium- to fine-grained, subarkosic sandstones (Fischer et al., 2007).

Heidsiek et al. (2020) reported that the reservoir quality of the formation is limited by the distribution of diagenetic cements, which are composed of poikilitic calcite, illite, and iron oxide grain coatings as well as K-feldspar and quartz overgrowths. ^{40}Ar–^{39}Ar laser spot dating of authigenic K-feldspar recognized two age clusters at 222±2 Ma and 186±14 Ma, respectively (Fischer et al., 2012). Based on the partial annealing of zircons, the rocks probably reached temperatures of 170–190°C before Late Cretaceous–Early Tertiary uplift (post 92 Ma). Although the illites at this location have not been dated, two clusters of illite ages have been reported in Rotliegend sandstones of the region with K-Ar age groupings of 210–180 Ma and 155–190 Ma (Zwingmann et al., 1998).

Measurements of intrinsic permeabilities of the sample block derived from the quarry ranged between 1.1 and 5.4 md using a helium permeameter (Jacob et al., 2021) and between 0.1 and 13.7 md using an air-permeameter (Heidsiek et al., 2020). The latter measurements also included local anomalies of up to 140.26 md, attributed to localized channel flow behavior.

Numerous cores with a diameter of 2.5 cm were drilled out of the 45 cm × 39 cm × 11 cm sample block (Fig. 1). These were located in both cross-bedded and laminated parts of the aeolian facies. To include the natural heterogeneity within the sedimentary layer, a set of 20 samples was extracted and sectioned into two consecutive discs each 5 mm thick. One of the discs was used for XRD study and the other for FIB-SEM investigations. Most FIB-SEM analyses were undertaken using the cores F4 and E6. The small-scale facies heterogeneity of the sample block and its impact on petrophysical properties was studied in detail by Heidsiek et al. (2020) and Jacob et al. (2021). However, as shown by investigations of quarry-wide thin sections reported by Fischer et al. (2012), the structures observed were considered to be representative of and characteristic of the cross-bedded and parallel laminated layers of the aeolian deposits of the Parchim Formation at this location.

Methods

X-ray Diffraction and Rietveld Refinements

The average bulk mineralogical composition of the aeolian sandstone layer was analyzed using 20 micronized powder samples (Fig. 1). For a detailed clay-mineral

study, the <2 μm size fraction was separated from a rock fragment (~100 g) by ultrasonic dispersion followed by gravitational settling. The illite fraction was then purified by first dissolving carbonate minerals using 0.3 M citric acid solution, and second by dissolving iron oxides using the citrate/bicarbonate/dithionite method of Mehra and Jackson (1960). Repeated centrifugation and redispersion was used to obtain a purified <1 μm size fraction. Between each centrifugation step, the >1 μm fraction at the base of the centrifuge tube was discarded and the clay-in-suspension redispersed using an ultrasonic bath. After seven repetitions, XRD quantification of the fine fraction separated thus, prepared as a random powder on zero-background sample holders, showed it to be ~95% pure illite with only traces of quartz and feldspar. The high purity of the separates was confirmed by transmission electron microscopy examination using a JEOL JEM-2100Plus instrument (Tokyo, Japan). The fraction was also analyzed as an oriented preparation on a glass slide to characterize in more detail the nature of the illite minerals. Note that the durations for the gravitational grain-size separation were determined by Stokes' law, which, strictly, is valid only for spherical particles. Nonetheless, diagenetic illite laths and fibers of 10+ μm lengths were still present in the separated and purified <1 μm size fraction.

XRD data were collected using a Bruker D8 Advance diffractometer (Karlsruhe, Germany) with CoKα radiation, a Lynxeye 1D stripe detector, and primary and secondary Soller collimators. Bulk samples were measured between 3 and 80°2θ using an aluminum sample holder and a fixed divergence slit with a 0.5° opening angle. The XRD pattern of the purified powder was obtained using zero-background sample holders, a variable divergence slit to avoid beam spilling, and a 6 mm radiated sample length. Oriented mounts were prepared with a load of 4 mg/cm^2 and measured between 3 and 40°2θ in the air-dried and ethylene glycol-saturated state.

Quantifications were performed by Rietveld full profile modeling using the BGMN/Profex software package (Bergmann et al., 1998; Doebelin & Kleeberg, 2015). Structure files were taken from the internal database. Additionally, an R0 illite-smectite interstratification model by Ufer et al. (2012) was used to model the PCI/1M_d illite structure. This model includes the quantification of n·60° and n·120° layer rotations as well as trans-vacant (tv) and cis-vacant (cv) layers and interstratified smectite. Bulk random powder Rietveld refinements were run with a fixed background polynomial of 5th order (RU=5) while purified pattern modeling was undertaken without background restrictions. XRD patterns collected using a variable divergence slit were divided by sin(θ) before refinement, which resulted in a reasonable approximation to fixed slit measurements.

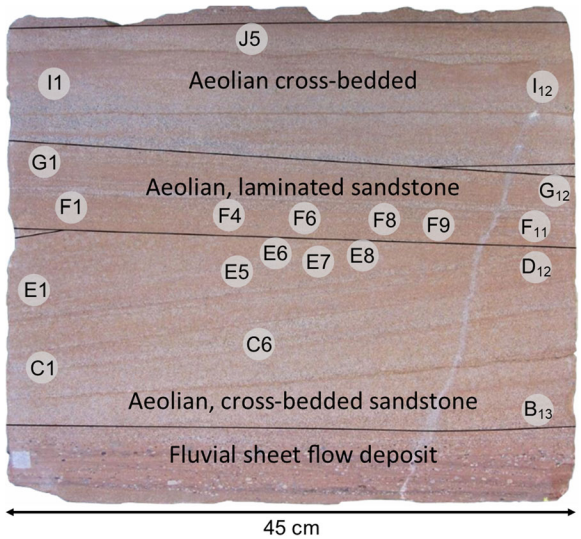

Fig. 1 Sample block with locations of drilled sample discs. Facies assignment is based on Heidsiek et al. (2020)

In addition to Rietveld refinements, the illite crystallite size distribution (CSD) of the <1 μm size fraction was determined by the Warren-Averbach method using the program *MudMaster* (Eberl et al., 1996). For analyses, the (002) basal reflection of illite was selected, which was obtained by a slow scan of a thin, oriented clay preparation. For the calculation, appropriate intensity corrections were made assuming a pure K-illite phase and by applying the autocorrection mode. The range for the Fourier analyses was 15–25°2θ and the quality of the results verified by examining the shape of the interference function. The lognormal parameters of the calculated CSD expressed as α and β are equivalent to μ and σ defined in Eq. 1 (see 'Pore-size distribution' below).

FIB-SEM

FIB-SEM was used to image the illite-specific, submicrometer porosity of the Rotliegend sandstone. The study was conducted with a Zeiss (Oberkochen, Germany) Auriga crossbeam field emission microscope with a Gemini electron and Orsay Physics (Fuveau, France)

FIB column. The ion-beam sectioning was performed at 30 kV with beam currents of between 1 and 2 nA and a feed between 25 and 35 nm for each slice. The exact settings were chosen depending on the pore structure and its susceptibility to curtaining artefacts. Polished sections were electron imaged at 1 kV with a secondary electron (SE2) detector to minimize charging artefacts. The internal microscope tilt correction was utilized to account for the 54° sample tilt. Slices were collected at an image resolution of 2048×1536 pixels. The voxel and image stack dimensions for each sample are given in Table 1. The elemental compositions of sites of interest were probed by energy-dispersive X-ray spectroscopy (EDX) using an 80 mm^2 Oxford Instruments (Wiesbaden, Germany) X-Max detector.

Image Processing and Segmentation

All image processing was undertaken using the Thermo Fisher software *Avizo 9.3* (Waltham, Massachusetts, USA). A workflow for the collected FIB-SEM image stacks was established to improve the geometry and image quality of the datasets. First, a pre-alignment of the image stack was carried out to decrease the coarse image shift along the sectioning direction. Subsequently, the dataset was cropped to remove information outside the imaging plane. Then a fast Fourier-transform filter was utilized to remove curtaining artefacts. A second slice alignment was performed resulting in a dataset without observable image translation. Shading artefact correction and a gray-scale histogram normalization along the milling direction were performed to correct for gray-scale fluctuations during the sectioning. Noise reduction was achieved using a non-local means filter in 2D mode to remove noise while preserving grain and pore edges.

The automated segmentation of pores in ion polished images was challenging due to the variety of artefacts that occurred along edges (electron charging) or with large pores (shine through artefacts). A recent study by Berg et al. (2018) demonstrated the advantages of machine-learning segmentation over conventional thresholding or watershed techniques. Jacob et al. (2021) utilized successfully the machine-learning software *Ilastik 1.3.3* (Berg et al., 2019) to segment pores in a highly porous FIB-SEM derived illite structure. In the present study, the *Ilastik* program and its 2D pixel classification workflow were used to mask the porosity of all analyzed structures. Therefore, training datasets for each volume were generated by combining conservative gray-scale thresholding and manual masking of the first and last slice of each volume plus every 100^{th} image. The resulting training mask included two phases: (1) the solid mineral matrix; and (2) the pores. After the segmentation, the labeled images were exported and transformed into binary images for further analyses.

Pore-size Distribution

The algorithm of Münch and Holzer (2008) was used to calculate 3D continuous pore-size distributions (PSD) from binary segmentation images and the total porosity (φ). The PSDs thus obtained showed a log-normal trend. To analyze further and compare the measured datasets, non-linear least-squares curve fitting was used to fit a probability density function (PDF) to the log-normal distributions. This approach allowed direct comparison of PSDs as they are independent of the total porosity (φ) and the volume analyzed. For porous media applications, Zydney et al. (1994) and references therein, showed that the general form of the PDF can be given as:

$$f(r) = \frac{1}{\sigma r\sqrt{2\pi}} exp\left(-\frac{(ln(r)-\mu)^2}{2\sigma^2}\right) \quad (1)$$

Where r is the pore radius; μ, the mean; and σ, the standard deviation. Note that μ and σ are the mean and standard deviation of the normal distributed variable ln(r) and not the PDF. By fitting μ and σ in Eq. 1 to the given pore-size distribution, the mean R_m of the pore-size distribution can be calculated by:

$$R_m = e^{\mu+\frac{\sigma^2}{2}} \quad (2)$$

the most probable pore radius R_p by:

$$R_p = e^{\mu-\sigma^2} \quad (3)$$

and the median R^* of the distribution by:

$$R^* = e^{\mu} \quad (4)$$

Modeling

To estimate the matrix flow properties of the connected pore systems within the analyzed structures, computational fluid dynamics (CFD) simulations were run by solving the Navier-Stokes equation on different

Table 1 Size properties of FIB-SEM volumes analyzed (*after processing, φ – total porosity)

Sample	Voxel size (*x*×*y*×*z*) (nm)	Grid dimension* (voxels)	Physical dimensions* (μm)
Meshwork illite	12.5×12.5×25	879×1043×370	11.0×13.0×9.3
Tangential illite	10×10×35	824×1298×73	8.2×13.0×2.6
Na-feldspar	17.5×17.5×35	951×930×297	16.6×16.3×10.4
K-feldspar (high φ)	12×12×35	1227×906×351	14.7×10.9×12.3
K-feldspar (low φ)	12×12×35	2236×1669×212	26.8×20.0×7.4

extracted sub-volumes. Calculations were realized using the *FlowDict* module of the software package *GeoDict* by Math2Market (Kaiserslautern, Germany). Simulations were run for water viscosity at 21°C. A pressure gradient of 100 Pa was applied between the inflow and outflow plane, and symmetric boundary conditions were defined for all other faces. Simulations were run in the *x*, *y*, and *z* directions successively. A detailed description of analogue calculations can be found in Jacob et al. (2021). Because the pore systems of the analyzed volumes are strongly heterogeneous and do not build up connected clusters across the analyzed volume, cubic domains with edge lengths between 192 and 384 voxels were extracted from the binarized pore-space models. This was undertaken in all volumes studied except for the tangential illite sample, where the whole coating region was treated as one computational domain. To achieve cubic domains, the binarized data were resampled to cubic voxel sizes in advance.

Results

X-ray Diffraction

The main mineral components of the Rotliegend sandstone are quartz, illite, feldspars (K- and Na-), and calcite (Fig. 2a, Table 2). Hematite and baryte occur in traces of <1 wt.%. Illite and calcite contents fluctuated widely, whereby low calcite often correlated with high illite content and vice versa. In most samples, two calcite generations were distinguished by their different *d*-spacings due to the enrichment of Mn in the youngest-generation calcite (Pedrosa et al., 2021).

Oriented aggregates of the purified <1 μm size fraction were used to determine the types of clay mineral present (Fig. 2b). The oriented patterns showed a 15 Å and a 10 Å phase. For the 10 Å illite phase, a shift of the 10.08 Å (001) reflection towards smaller *d*-spacings (9.92 Å), together with an intensified asymmetry towards smaller diffraction angles, was observed after EG saturation. The (002)-spacing (4.97 Å) did not change significantly and the (003)-spacing (3.31 Å) increased slightly to 3.32 Å. The basal spacing of the 15 Å phase increased to ~17 Å after EG treatment, which is characteristic of a two water-layer smectite containing a bivalent interlayer cation (e.g. Ca^{2+} or Mg^{2+}).

The reduced intensity of the 10 Å (001) reflection combined with the increase of intensity of the 3.3 Å (003) reflection after EG saturation was attributed to small amounts of intercalated smectite layers. Based on the intensity ratio of the (001)/(003) reflections for the air-dried and EG saturated states, a value of 1.4 suggests an average of 4% interlayered smectite occurred in the illite crystals (Moore & Reynolds, 1997; Środoń & Eberl, 2018).

The XRD patterns of the purified <1 μm fraction combined with quantitative Rietveld refinements were used to determine illite polytypes. This fraction contains only minor amounts of accessory phases with 4 wt.% quartz and 3 wt.% feldspars. Smectite was not observed in random powder patterns, and thus not included in the refinements. The XRD pattern (Fig. 3) showed two illitic phases: (1) a trans-vacant 1*M* polytype and (2) a disordered $1M_d$ illite. The $1M_d$ illite is characterized by broad reflections and an "illite hump" in the angular region between 22 and 46°2θ (green line in Fig. 3b) (Grathoff & Moore, 1996). The refined $1M_d$ model consists of 64% tv and 36% cv layers. The probability *p0* for 0° rotations reached the lower boundary value of 1/3, equivalent to a maximum degree of disorder. The probability for rotations of $n{\cdot}60°$ is 0.17 and for $n{\cdot}120°$ is 0.49. The amount of interstratified smectite layers was 5%, which was consistent with the oriented aggregate result. The $1M_{tv}$ illite was identified by its sharper overlaying reflections (i.e. $(\overline{1}\,\overline{1}\,1)$: 4.35 Å, $(\overline{1}\,1\,2)$: 3.65 Å, (112): 3.07 Å) that do not match the broad peak shape of

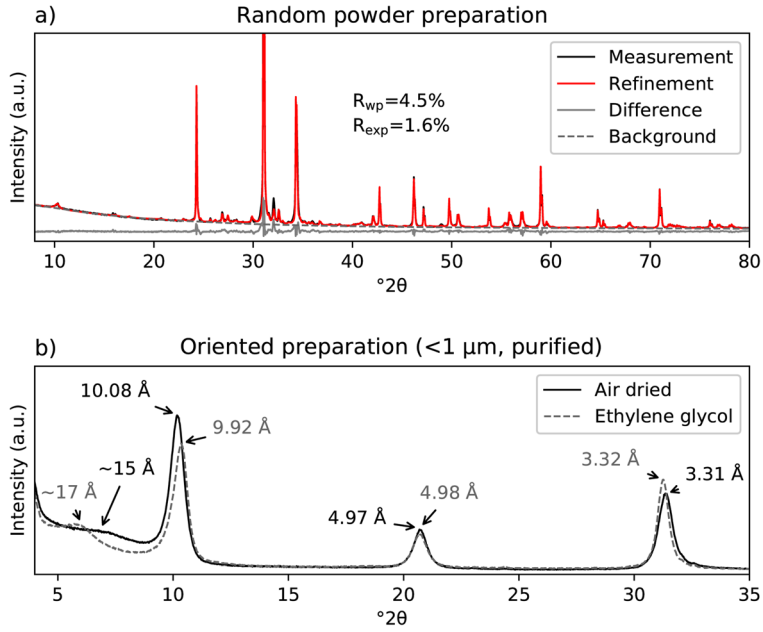

Fig. 2 **a** Rietveld refinements of the random powder preparations of the micronized bulk material. **b** Oriented aggregate of the purified fraction in air-dried (AD) and ethylene glycol-saturated (EG) state

the underlying $1M_d$ polytype. For the $1M_{tv}$ structure, crystallite size peak broadening and microstrain were refined. The total weight fractions were 77 wt.% $1M_d$ and 16 wt.% $1M_{tv}$ illite for the purified <1 µm fine fraction.

Calculations of the illite CSD for the purified <1 µm size fraction obtained using the *MudMaster* program by Fourier analyses of the (002) reflection produced a thickness distribution of crystallites (Eberl et al., 1996). These ranged (in the crystallographic *c* direction) between 1 and 80 nm. The average illite crystallite thickness was 24.7 nm with log-normal parameters of µ = 2.89 and σ = 0.77.

Microscopy

The SEM analyses of rock fragments and ion-polished surfaces revealed the diversity of illite-related textural and structural features whereby analyses of rock fragment showed an undisturbed image of delicate illite structures within the open pore space. The distribution of illite structures and the relationship between feldspar alteration and illite growth were studied further by light microscopy imaging (Fig. 4). Three types of illite textures were observed: (1) as illites replacing K-feldspar grains and meshwork textures; (2) as grain coatings (cutans or tangential illites); and (3) as pore fillings between grains.

K-feldspars occurred as detrital grains and diagenetically grown cement, both of which were associated with extensive secondary porosity caused by dissolution and nanocrystalline cement precipitates (Figs 5a and 7a). Na-feldspars (albite) occurred only as cements and contained unfilled porosity. In contrast, in most K-feldspars, grain-replacing illite crystals were observed. Calcite precipitated commonly within the pore space of K-feldspar grains (Fig. 5b). The surface structure of K-feldspar grains showed two specific characteristics: (1) illite crystals that extended out of altered K-feldspar grains to form thin sheets around most of the K-

Table 2 Average mineralogical composition of the aeolian Rotliegend sandstone layer analyzed (n = 20, SD – standard deviation)

	Quartz	Na-Feldspar	K-Feldspar	Calcite	Hematite	Baryte	Illite
Mean (wt.%)	63.7	7.6	8.6	5.9	0.5	0.5	13.2
Minimum (wt.%)	57.4	4.5	7.1	1.1	0.3	0.2	10.3
Maximum (wt.%)	68.5	9.6	10.2	18.2	0.7	1.3	15.9
SD 2σ	5.1	2.6	1.7	8.6	0.2	0.6	3.1

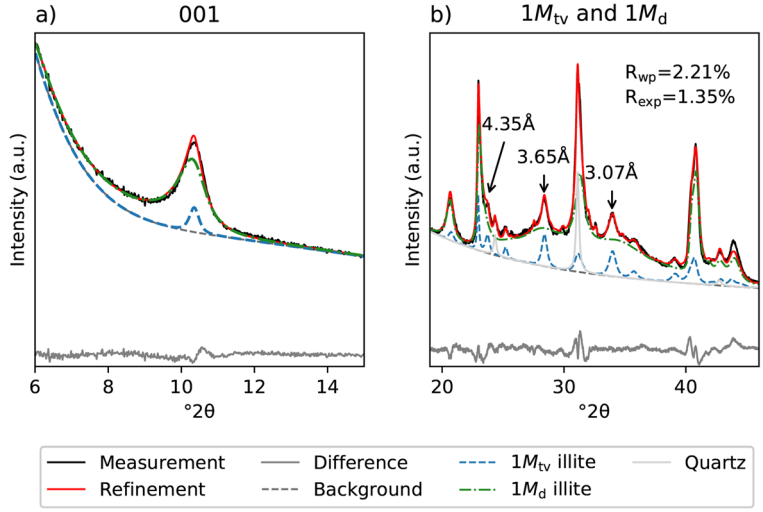

Fig. 3 XRD patterns and refined Rietveld model of the purified <1 μm size fraction. **a** The $1M_{tv}$ (001)-reflection is sharper with a slightly smaller *d* spacing compared to the $1M_d$ (001) spacing. The larger spacing of the disordered reflection is caused by minor amounts of interstratified smectite. **b** Decomposition of the angular range between 19 and 46°2θ. $1M_{tv}$ polytype specific peaks are highlighted

feldspar grain surfaces (Fig. 5c); and (2) layers that were formed by aggregated lath-shaped crystals that were interconnected to form sheets (Fig. 5d). The orientation of the crystals to each other appeared to be random. Hematite crystals <100 nm in size were often found on top of these layers.

Illite meshwork structures formed grain replacements >100 μm in size and extended commonly over the initial grain boundaries and grew into the intergranular pore space (Fig. 5e). These curly illite crystals formed honeycomb-like structures with lenticular- to slit-shaped internal pores (Fig. 5f). In some regions, these structures had a preferred tangential orientation surrounding grains. Compared to other honeycomb structures, which are observed commonly in other illite-bearing sandstones (Weibel et al., 2020), the thickness of the twisted sheets is >100 nm. Crystals observed on the surface of these sheets were flaky and had irregular shapes. Dissolved K-feldspar remnants were observed commonly within these structures.

Polished specimens and thin sections showed quartz and feldspar grains that were sub-rounded to rounded. Grain coatings were observed along most grain boundaries (Figs 4 and 6a). These coatings were formed by μm-thick layers of illite particles (Fig. 6b–d), which are often referred to as tangential illites (Desbois et al., 2016). Menisci between two coatings were observed rarely. Coating growth was also seen around authigenic microquartz crystals (Fig. 6c). The outer visible layer of the coating was covered by idiomorphous lath- to hexagonal-shaped illite crystals (Fig. 6b, c). The coating thickness was greater in intragranular and angular regions and was frequently thicker in regions with no calcite cementation. In regions with poikilitic calcite,

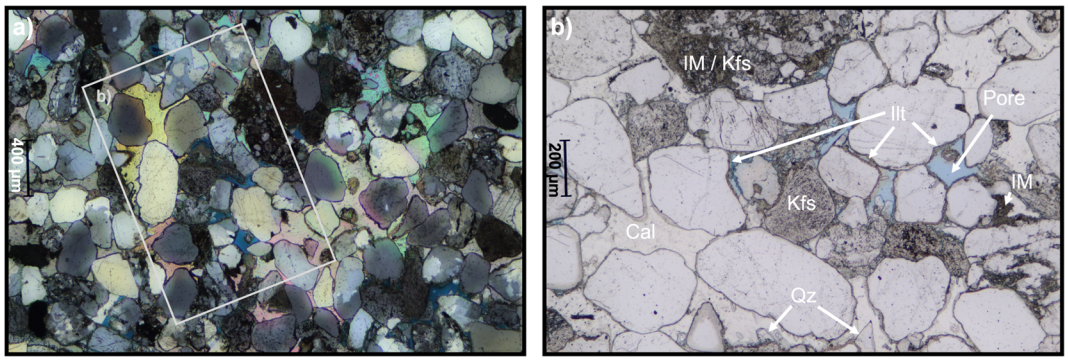

Fig. 4 **a** Cross-polarized thin section micrograph showing the distribution and thickness of illite grain coatings and poikilitic calcite cement. **b** Illite coatings in open pores are often thicker and cover whole grain surfaces whereas coatings in areas of poikilitic calcite are generally thinner and visibly enriched in grain depressions and on rough grain surfaces. Cal – calcite, Kfs – K-feldspar, Ilt – illite, IM – illite meshworks, Qz – quartz. Abbreviations after Warr (2020)

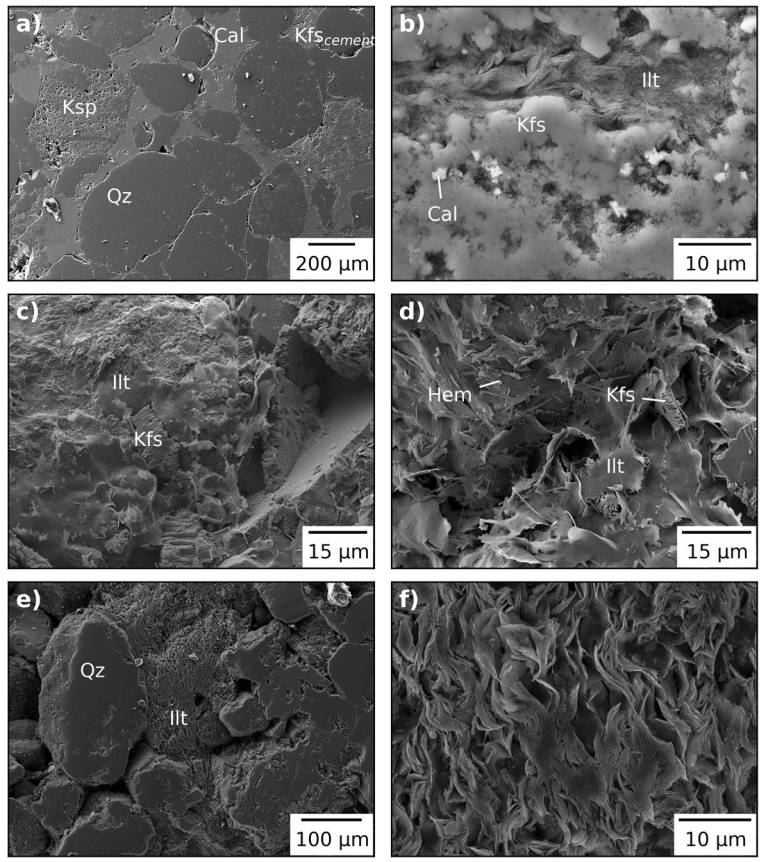

Fig. 5 **a** Hand-polished surface of Bebertal sandstone showing the diversity of diagenetic textures. As well as large poikilitic calcite (Cal) cements, K-feldspar (Kfs) and quartz (Qz) cements are common. Both Kfs detrital grains and cements show alteration to meshwork illite. **b** Close-up of a polished section of a diagenetically altered Kfs grain. Within the pores of the grain, Cal and illite (Ilt) precipitates are common. **c** Fractured rock fragment image showing an altered Kfs grain surface. Thin sheets of lath-shaped Ilt have grown and cover large parts of the Kfs grain surface. **d** Aggregated Ilt laths occupying the intergranular pore space. Hematite nanoparticles are commonly observed on these layers. **e**, **f** Hand-polished section of illite meshworks that form honeycomb structures with thick curly Ilt sheets. Irregular crystals were observed in these pore-filling structures that predate the Ilt laths and fibers. Abbreviations after Warr (2020)

thinner coatings were observed on smooth quartz surfaces, which thicken commonly with increasing surface roughness (Fig. 4b). Pores are notably common at the interface between angular quartz grains and the coating. At the interface between K-feldspar and the tangential illite, illitized K-feldspar was common (Fig. 6d). Crystals on grain coatings seemed to be oriented randomly; however, the image resolution used in this study was not sufficient to determine potential nucleation sites.

Pore-filling illite had idiomorphous fibrous- to lath-shaped crystal habits that extended commonly from the illite substrate into the open pore space. Within these assemblages, the crystal sizes and shapes were notably homogeneous (Fig. 6e). Crystals were elongated along the crystallographic *a* axis and reached lengths of up to 50 µm with breadths of up to 2 µm along the *b* axis (Fig. 7b). Between the different pores, crystal sizes varied, especially in the *b* direction. The agglomeration of laths to form crystal mats was observed frequently. Pore-bridging fibrous crystals that nucleated on illite coatings were common near grain contacts (Fig. 6f).

Elemental Analyses

The EDX analyses of the different types of illite were performed on selected FIB-SEM ion-polished sections. Each of the textural varieties described was analyzed, namely the illite replacing K-feldspar, meshwork illite, and the grain coating of illites (Table 3). Only the fibrous pore-filling illites could not be measured. To reduce interference from surrounding mineral grains, EDX maps were collected on hand- and ion-polished sites that appeared homogeneous. No maps were collected in the vicinity of calcite grains. As no Ca-feldspar was present in the samples, the observed calcium was assigned to intercalated Ca-smectite in the illite crystals. Some of the spectra from illite may have been contaminated by signals from surrounding grains, however, because the volume of X-ray generation exceeds the size of the analyzed illite structures. Further inaccuracies may arise from surface roughness. EDX measurements of the purified <1 µm fraction were also acquired for comparison. An idealized structural formula for this sample was calculated and is presented in Table 3.

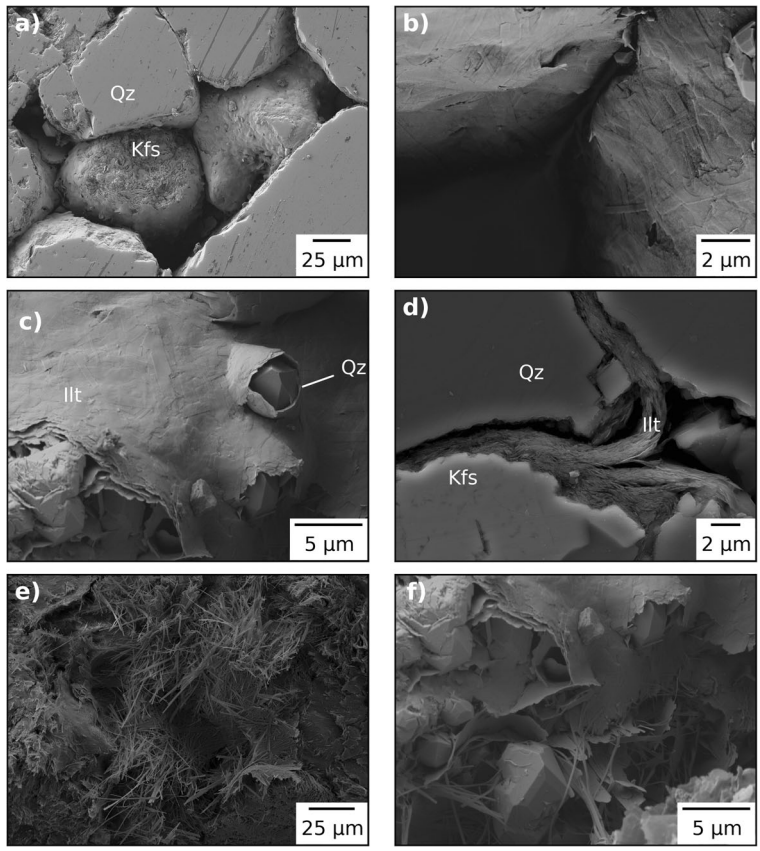

Fig. 6 **a** Hand-polished section of uncemented detrital grains, including the altered K-feldspar (Kfs) grain containing grain-enveloping coatings of illite. **b** Contact areas between two detrital quartz grains that are covered by illite coatings comprised of interlocking lath-shaped crystals. Menisci between coatings are rarely observed. **c** Open pore spaces with the growth of illite coating around authigenic microquartz crystals. Pore-bridging illite fibers in the lower region of the image (f) are seen to post-date the quartz crystals. **d** Polished section showing a junction between three grains. Pores are commonly found between the quartz (Qz) surface and the coating. No pores were found between Kfs surfaces and illite coatings. **e** Illite lath- to fiber-shaped crystals growing into open pores. The laths are often stacked together to form dense and twisted mats. **f** Pore-bridging laths and fibers that nucleate on illite substrate. Abbreviations after Warr (2020)

Overall, the measured compositions appeared very similar. Values that differed substantially from the purified <1 µm analyses could be attributed to contaminations of the grain-size assemblage used which contained traces of quartz and feldspar. Elevated K_2O values of the illites in K-feldspars and the meshwork illites were probably caused by the presence of K-feldspar grains and their remnants. The elemental data of the coating illites showed the greatest variability with large fluctuations in FeO, K_2O, and SiO_2 contents probably caused

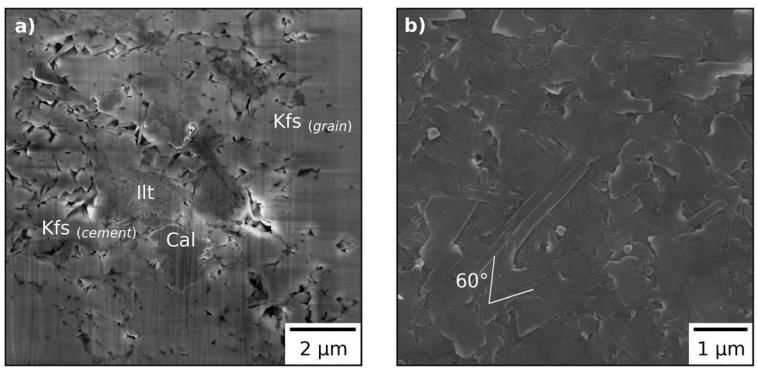

Fig. 7 **a** SE image of an ion-polished section scanned at 5 kV of the low φ K-feldspar (Fig. 8e) which shows structural features such as illite (Ilt) distribution and K-feldspar (Kfs) and calcite (Cal) precipitates. After a period of feldspar dissolution, the second generation of K-feldspar cements partially filled the generated pore. Subsequent calcite and illite precipitation further decreased the pore volume within the grain. IntraP and InterP pores occur mainly in the feldspar matrix. **b** Crystal shape analyzed on the purified illite fraction. Elongate, lath-shaped to fibrous crystals are common. 120° growth steps indicate a surface spreading growth mechanism

by the various substrates on which these structures were found. The largest FeO values were probably caused by hematite accumulations and the increased SiO_2 values by quartz substrates. Meshwork and coating illites showed no Na_2O whereas CaO was observed throughout all samples and probably reflected some intercalation of smectite layers within the minerals. Structures without Na_2O showed notably higher CaO values suggestive of varying smectite interlayer compositions. The composition of illite in K-feldspar differed least from the bulk purified fraction that was analyzed.

Pore-structure Analysis

Five nanoporous zones were identified that are characteristic of the studied Rotliegend sandstone. For each of the five zones, locations were chosen for FIB-SEM serial sectioning and 3D reconstructions (Table 1). A typical secondary electron (SE) image for each analysis is shown in Fig. 8 and 3D renderings of each volume including the segmented pore space are plotted in Fig. 9. Most nanoporous structures can be related to the occurrence of illitic clay minerals and feldspar cements. Pore structures are described based on the classification of Loucks et al. (2012), which differentiates between intraparticular (IntraP) and interparticular (InterP) pores.

Meshwork illites were uncommon but were the largest structures observed with the spatial dimension of >100 μm and high total porosities as shown in Figs 8a and 9a–c. These structures were found (1) as grain replacements of K-feldspar grains and (2) as replaced K-feldspar cements indicated by their intragranular occurrence. The characteristic of this type of pore structure was slit- and triangular-shaped pores, which were found within and between distinct clay mineral lamellae. Within these structures, InterP pores were visually larger than IntraP pores. Because these types are often interconnected within larger 3D pore clusters, however, the transitions cannot be defined clearly. A recurring feature in these regions was the twisted thin curly illite crystals that nucleated within and around K-feldspar grains the remnants of which were often <1μm in size. An example of a cross-section of this type of structure can be found in the InterP pores of Fig. 8a. Meshwork illites form well connected nanoporous clusters that appear evenly distributed.

Na- and K-feldspar both contained significant amounts of porosity. The absence of diagenetic illite crystals within its pore space was characteristic of Na-feldspar (Fig. 8c). The reconstructed volume contained ~5.1 vol.-% porosity, which was aligned along the cleavage planes of the feldspar. These types of structures were exclusively IntraP pores. The Na-feldspars analyzed showed the largest range of pore sizes with radii of >1 μm (Fig. 10). The connectivity of these pore clusters was low with no axis connectivity at the observational scale, however. Porosity within Na-feldspar is, therefore, likely to be primary and developed during the formation of the cement.

In contrast to Na-feldspars, K-feldspars contain secondary porosity. Generally, the porosity in K-feldspars is caused by feldspar dissolution and feldspar and illite precipitation. The porosity observed in the present study had a channel structure and was distributed heterogeneously within the dissolved feldspar grain volume (Fig. 9j–o). The total porosity in the K-feldspar grains varied between 3 and 6.7 vol.%. Various types of pore shapes and sizes could be distinguished based on the total porosity of these grains (Fig. 9d–f). High φ grains showed complex pore shapes with systems built up by InterP- and IntraP-illite pores. The illite particles in these subsystems were thin platy to fibrous in habit. The associated pores were irregularly shaped and differed in size. The degree of connectivity within these clusters was high (Fig. 9l). Low φ grains contained less diverse shapes. Two main types of structures were found: (1) IntraP pores in K-feldspar caused by dissolution and/or the precipitation of tiny K-feldspar cement crystals; and (2) InterP/IntraP pores associated with illite precipitates. The latter were dominated by slit to triangular-shaped pores. Further, calcite precipitates were found within regions dominated by K-feldspar cement pores (Fig. 5b).

Tangential illites formed grain coatings around the borders of detrital grains. The characteristic of these rims were low internal porosities (<1 vol.%) and pores that were frequently filled with hematite (Fig. 8a,b). The rim thickness was up to 1 μm in regions with early diagenetic cements and visibly larger in open pores (Fig. 6a). Between tangential illites and the early diagenetic poikilitic calcite cement, slit-shaped pores were common. Tangential illite structures showed the lowest total porosity and the lowest degree of connectivity out of all analyzed structures.

A transition from the grain coating tangential illite into meshwork illite was recognized in some cases with a zone 2–3 μm thick. These areas were characterized by low pore cluster connectivity but large pore and illite laminae sizes (Figs. 8a and 9a–c).

Table 3 Energy dispersive X-ray analyses (values ± 2σ standard deviation, n.d. – not detected)

	Na_2O	MgO	Al_2O_3	SiO_2	K_2O	CaO	FeO
Meshwork Ilt (N=5)	n.d.	1.6 ± 0.1	29.4 ± 0.3	52.9 ± 0.4	11.0 ± 0.3	0.7 ± 0.2	4.4 ± 0.4
Ilt in Kfs (N=9)	0.12 ± 0.07	2.4 ± 0.8	29.0 ± 1.8	55.2 ± 1.4	9.1 ± 0.3	0.5 ± 0.3	3.6 ± 1.0
Coating Ilt (N=4)	n.d.	0.9 ± 0.3	20.1 ± 3.5	61.6 ± 5.4	9.3 ± 2.9	1.0 ± 0.1	7.3 ± 4.4
Purified <1 μm (N=11) *	0.35 ± 0.05	2.2 ± 0.1	28.9 ± 0.2	56.6 ± 0.3	8.3 ± 0.2	0.3 ± 0.1	3.4 ± 0.1

*corresponding formula unit: $Ca_{0.07}Na_{0.04}K_{0.64}(Al_{1.53}Fe_{0.38}Mg_{0.09})[Si_{3.45}Al_{0.55}]O_{10}(OH)_2$

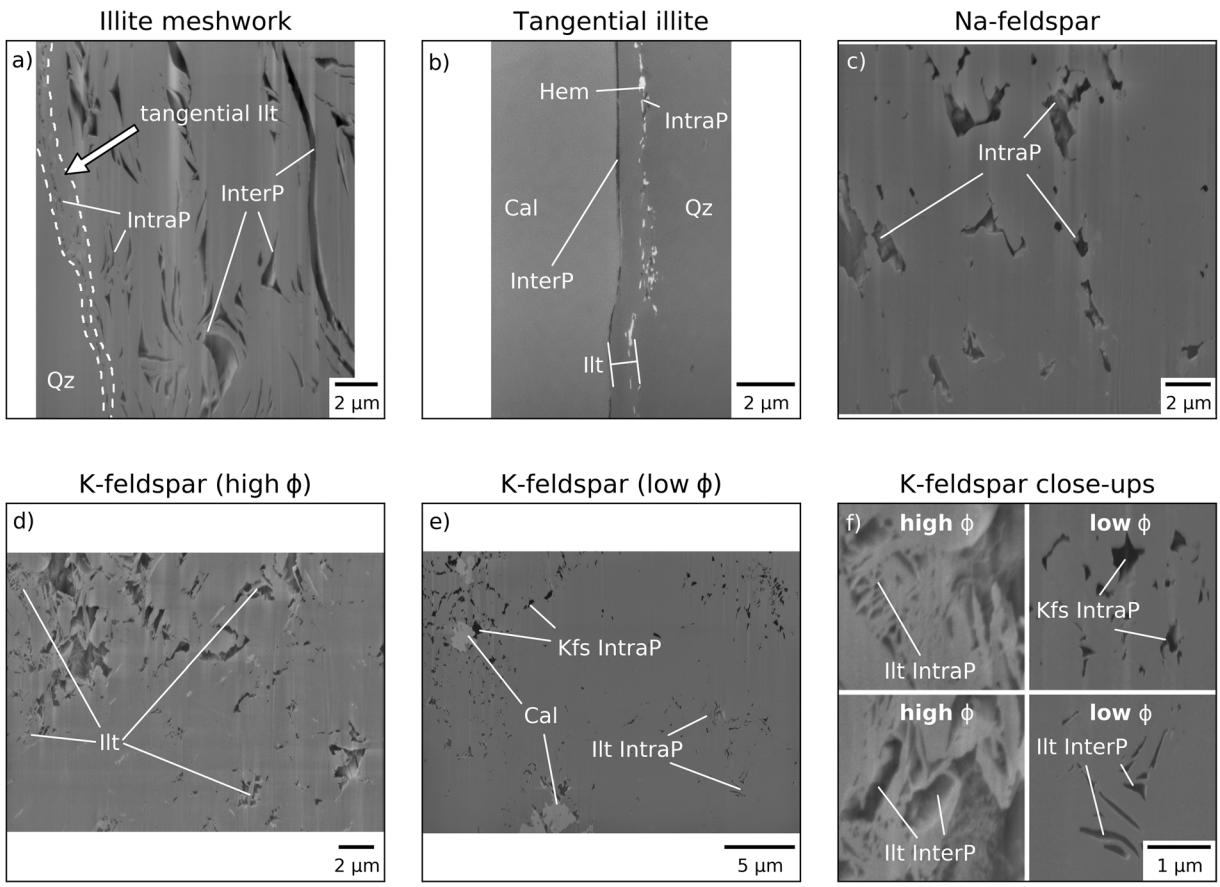

Fig. 8 Selected slices of FIB-SEM volumes. **a** Illite (Ilt) meshwork structures show predominantly slit- to triangular-shaped pores of varying size. These structures evolve from grain coating tangential illite. Twisted thin radial illite structures are marked in the bottom part of the image. **b** Tangential illite covers all detrital grain surfaces and shows little to no internal porosity. Slit-shaped pore structures between calcite (Cal) cement and illite point toward pressure dissolution or minor shrinking. Tangential illite is commonly cemented by Fe-oxides. **c** Na-feldspar shows large pore sizes that are oriented along crystal planes. No connectivity of pores was observed at the scale used, however. **d–f** K-feldspars (Kfs) are heavily altered with a deep-reaching pore system. The pore structures are diverse, depending on the type of pore filling. Kfs cement within Kfs grains is common and intraparticle (IntraP) pores are irregularly shaped. Pores related to illite depend on the amount of precipitated illite. Highly porous structures are dominated by IntraP and interparticle (InterP) with larger pore radii and irregular shapes. Heavily cemented areas show slit- to triangular-shaped pores. Abbreviations after Warr (2020)

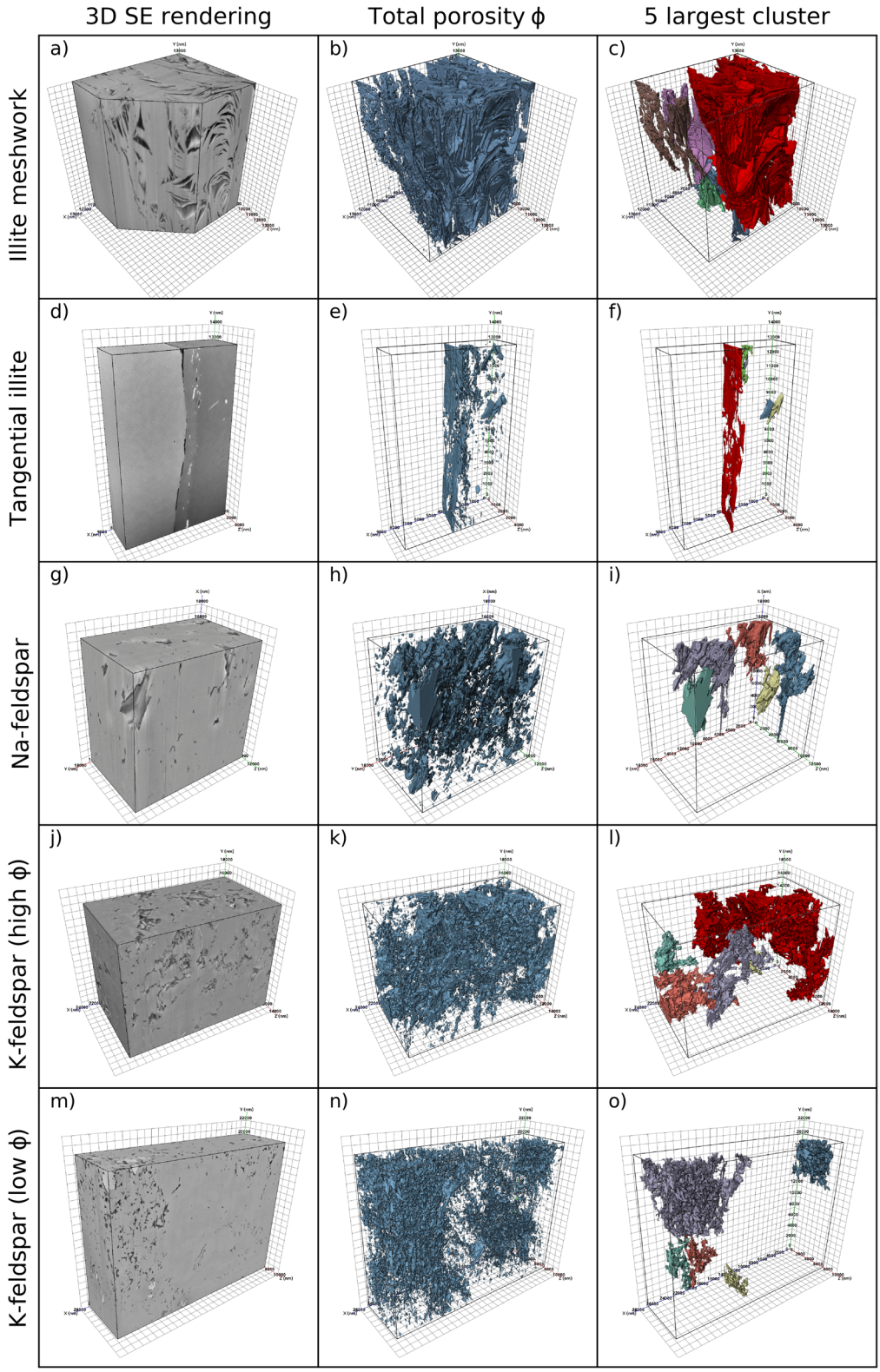

Fig. 9 Comparison of analyzed FIB-SEM structures. The left column displays 3D renderings based on SE images, the middle column a rendering of the extracted pore structure and the right column the five largest pore clusters, where axis-connecting clusters are shown in a deep red color (**c**, **f**, **l**). No axis connectivity was observed for Na-feldspar and K-feldspar (low φ)

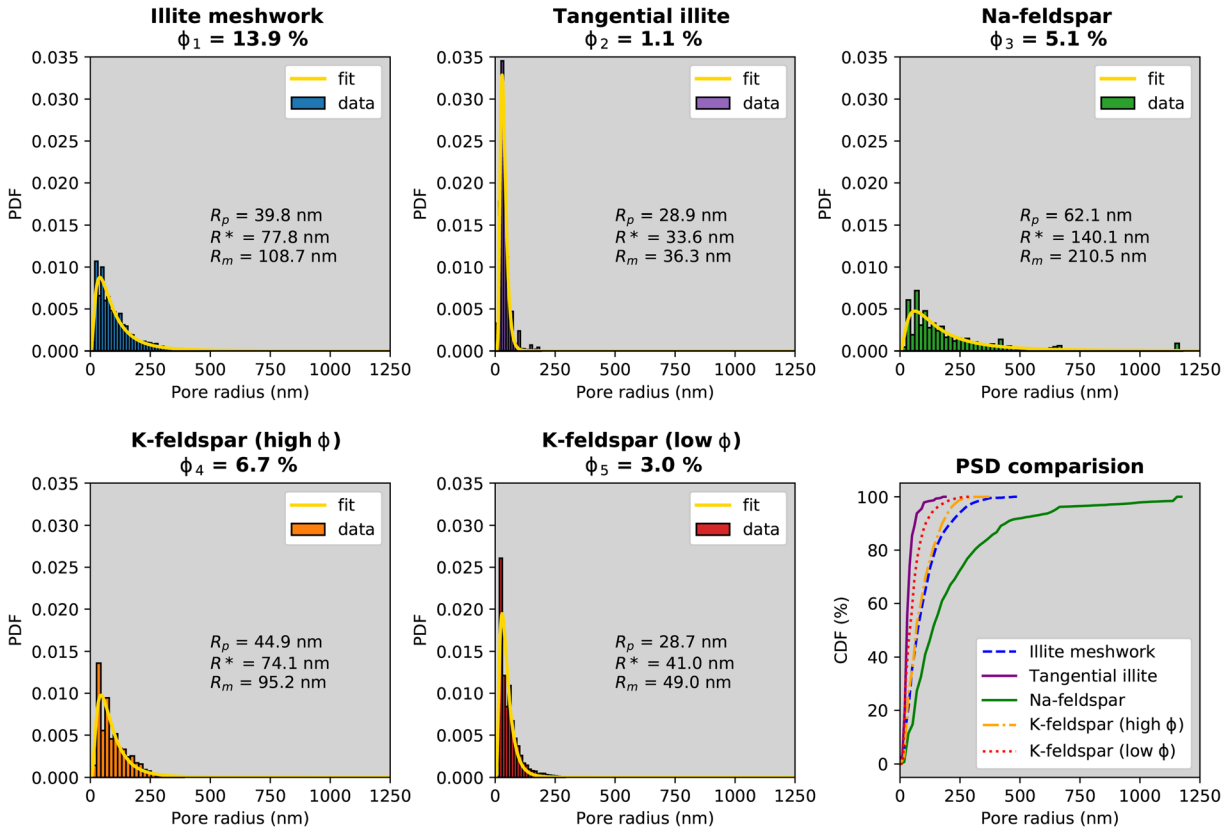

Fig. 10 Calculated geometric continuous PSDs of all five FIB-SEM pore space models plotted as probability density functions (PDFs). The yellow line shows the fitted log-normal curve. The illite meshwork and the Na-feldspar structures show the largest distribution of pore radii and the largest mean pore radii (Table 4). The bin-size is determined by the voxel size

Pore-size Distributions

The measured and calculated pore-size distributions as well as the results of the fitted PDF are shown in Table 4 and Fig. 10. The narrowest range of pore sizes combined with the lowest total porosities was associated with the tangential illites. The total porosity of this analyzed volume was 1.1 vol.%. The most probable pore radius was 28.9 nm, and the mean value was 36.3 nm. Note that most pore voxels in this structure were associated with a large slit-shaped pore network between the coating and the calcite cement and not within the actual coating itself (Fig. 9f). Low φ K-feldspars showed a similar R_p value (28.7 nm), but the range of pore radii was much larger as indicated by a higher median radius R* of 41.0 nm. Additionally, the illite meshwork and high φ K-feldspar structures showed similar pore-size statistics. The R_p values were slightly lower in illite meshworks (39.8 vs. 44.9 nm) but the pore-size range was marginally larger (R_m: 108.7 vs. 95.2 nm). Visually, this trend can be seen in the cumulative distribution function (CDF) plot in Fig. 10. The main difference between the two structures was the total porosity, which was more than two times higher in the illite meshwork compared to the high φ K-feldspar (13.9 vs. 6.7 vol.%). Na-feldspar showed the largest pore radii (R_p: 62.1 nm, R_m: 210 nm).

Permeability Simulations

The sub-domains for computational fluid dynamic simulations were extracted from the binarized resampled pore space volumes. As previously indicated, the analyzed volumes do not represent homogeneous pore systems. This is because they are either located within one mineral grain (Na- and K-Feldspar) that was subject to dissolution and precipitation during its burial history or within a mineral assemblage (e.g. tangential illites). Therefore, these pores are concentrated within certain regions. By extracting sub-domains from these areas,

Table 4 Fitted curve parameters, μ and σ (detailed description in section 'Pore-size distribution'), and statistical radii values for log-normal pore-size distribution curves

Sample	μ	σ	R_p (nm)	R^* (nm)	R_m (nm)	Φ (%)
Illite meshwork	4.35	0.82	39.8	77.8	108.7	13.9
Tangential illite	3.52	0.39	28.9	33.6	36.3	1.1
Na-feldspar	4.94	0.90	62.1	140.1	210.5	5.1
K-feldspar (high φ)	4.31	0.71	44.9	74.1	95.2	6.7
K-feldspar (low φ)	3.71	0.60	28.7	41.0	49.0	3.0

μ mean, σ standard deviation, R_p most probable radius, R^* median radius, R_m mean radius, Φ total porosity

generating connected pore clusters was possible. Modeled permeabilities are, therefore, not representative of the whole rock, but instead, provide information on matrix flow paths of various textural domains relevant to the circulation of diagenetic fluids.

Numerical calculations of permeabilities ranged between 0.1 and 13.4 μd (Table 5). Illite meshwork values varied between 0.1 and 6.2 μd with a noticeable enhancement in the *y*-direction. No flow was recognized in the *x*-direction in the tangential illite sample as it represents the direction perpendicular to the layered coating. Values in the *y*- and *z*-directions ranged between 0.1 and 1.4 μd. The tangential illite structure was the most heterogenous volume analyzed because it contained solid voxels of the surrounding calcite and quartz grains. The high-φ K-feldspar values ranged between 0.7 and 2.2 μd. The low-φ K-feldspar samples showed the greatest anisotropy within the modeled data with values between 0.1 and 13.4 μd (note that ROI6-8 partially overlap). These pore clusters were chosen because no further sub-domains $>256^3$ voxels existed within the dataset.

Discussion

Based on the results presented, a conceptual model summarizing the evolution of illite neocrystallization and the development of nano-porous systems in the Bebertal sandstone is illustrated in Fig. 11. The various aspects of the sandstone's diagenetic reactions, pore-size characteristics, and porosity-permeability evolution are discussed in the context of its geological history, as outlined in the thermal burial model of Fischer et al. (2012; fig. 8).

New Constraints on the Diagenetic History and Pore Evolution of the Bebertal Sandstone

According to the diagenetic sequence proposed by Fischer et al. (2012), the oldest generation of feldspar cement in the Upper Rotliegend sandstones was associated with a period of enhanced fluid flow following the rapid burial of the sandstone during Late-Permian to Early-Triassic times. The subsequent intense dissolution of feldspar grains and cements led to the formation of

Table 5 Results of CFD simulations run on extracted sub-domains. No flow path exists in the *x*-direction of tangential illite as it is the direction perpendicular to the coating surface

Sample	ROI	Domain size *x y z*	k_{xx} (μd)	k_{yy} (μd)	k_{zz} (μd)
Illite meshwork	1	384^3	0.1	5.0	1.5
Illite meshwork	2	384^3	0.6	6.2	0.3
Tangential illite	3	212×1298×256	no path	0.1	1.4
K-feldspar (high φ)	4	384^3	0.7	2.0	2.2
K-feldspar (high φ)	5	256^3	no path	1.1	1.4
K-feldspar (low φ)	6	384^3	0.2	9.4	1.2
K-feldspar (low φ)	7	384^3	0.1	10.0	1.1
K-feldspar (low φ)	8	384^3	0.3	13.4	1.1

ROI region of interest

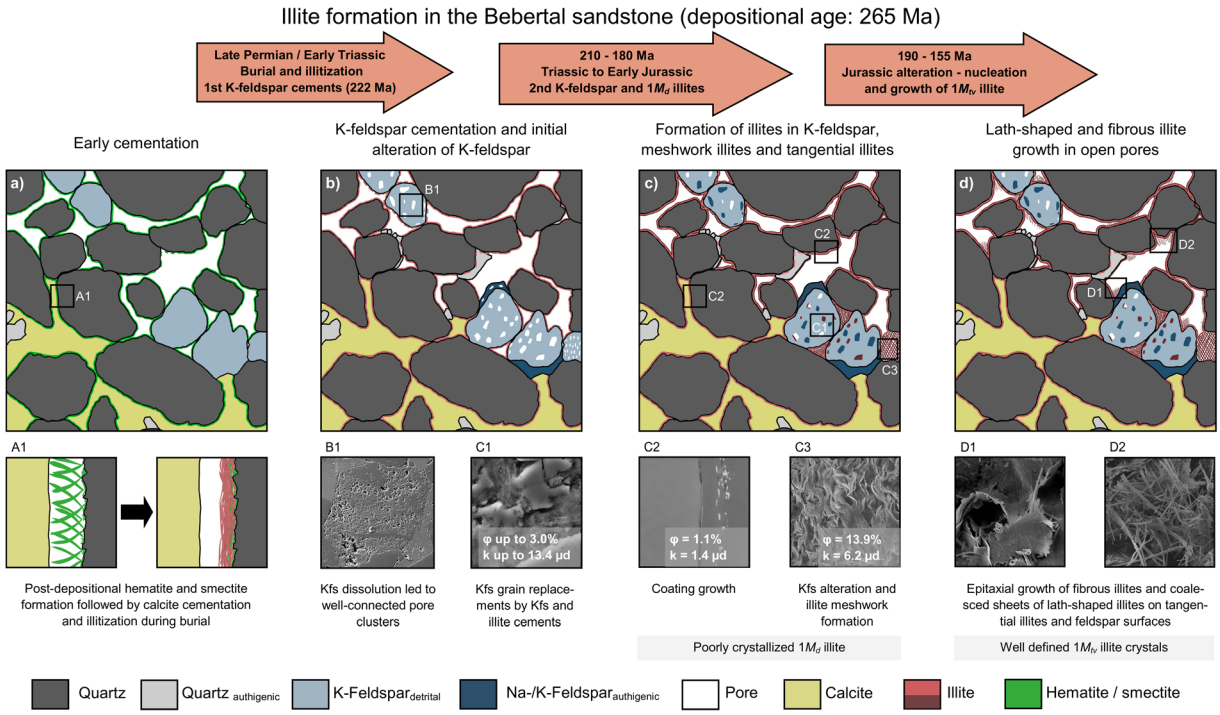

Fig. 11 Schematic diagram illustrating the development of illite-related porosity in the Bebertal sandstone. **a** Post-depositional hematite and smectite formation led to the development of thin initial grain coatings, which were subsequently illitized and compacted during burial. **b** Late Permian to Early Triassic K-feldspar alteration was characterized by the dissolution of detrital grains and the formation of authigenic K-feldspar and K-feldspar-replacing illite which all contain nano-porous pathways for diagenetic fluids. **c** As K-feldspar cementation faded, illite precipitation led to the formation of thin tangential coatings and illite meshwork structures. Meshworks formed within highly porous K-feldspar grains and as K-feldspar grain replacements. **d** The youngest generation of illites is composed of lath- to fiber-shaped crystals that nucleated preferably on older illite substrates and K-feldspar surfaces

large intragranular pore networks with local diameters of several micrometers (Fig. 11b). These networks, which formed in K-feldspar (Fig. 9), probably enhanced the flow properties of the reservoir at that time. This stage of dissolution and strong alteration of detrital K-feldspar grains with cement overgrowths resulted in authigenic ^{40}Ar-^{39}Ar ages of 222±2 Ma (Fischer et al., 2012).

The younger, second generation of K-feldspar cement dated at ~190–180 Ma (Fischer et al., 2012) indicates that a second mineral precipitation event affected these rocks, which has been linked to a Triassic to Early Jurassic phase of increased tectonic activity with the influx of hydrothermal K-rich fluids (Gaupp et al., 1993; Zwingmann et al., 1998). This stage of mineral formation probably reduced the secondary porosity by further K-feldspar cementation. This can be observed in the analyzed K-feldspar grains in regions with high porosities and irregularly shaped InterP pores. These regions are filled with K-feldspar cement composed of nm-sized crystals (Fig. 7a). Similar structures were described by Weibel et al. (2019) who attributed these to an abrupt supersaturation of the pore fluids with K.

Although the illites in this sample have not yet been dated, the occurrence of these minerals within K-feldspar grains, the illite meshworks, and the tangentially arranged platy illite coatings probably corresponds to the older group of illites described in the Rotliegend sandstone of this region. These have been dated as late Triassic to Early Jurassic with K-Ar ages in the range 210–180 Ma (Zwingmann et al., 1998) and crystallized following the previously described second generation of Jurassic K-feldspar cementation (Fig. 11c). That a second influx of K-rich fluids was responsible for both the younger generation of authigenic K-feldspar cement and the illite crystals found in and around K-feldspar grains (including meshworks and grain coatings) is partially supported by the general similarities in chemical composition and high concentrations of K. Crystallization probably commenced with K-feldspar growth and was

followed by some calcite precipitation as described by Heidsiek et al. (2020). This is confirmed by the observed intragranular K-feldspar and calcite precipitates (Fig. 5b). As the $a(K^+)/a(H^+)$ activity ratio decreased either by the precipitation of K-feldspar or by decreasing K^+ supply, conditions favored the precipitation of illite (Yuan et al., 2019). Based on the small number of intercalated smectite layers, as indicated by the elemental composition analyses and the irregular shapes of crystals edges, the replacement of K-feldspar grains, the illite meshwork textures, and the first generation of tangential coatings are all suggested to be composed of $1M_d$ illite.

The tangential illite coatings around detrital grains are an omnipresent feature of the Bebertal sandstone. In the literature, the origin of tangential clay coatings is often related to the mechanical infiltration of colloidal smectite-rich suspensions (Storvoll et al., 2002). However, based on the textural findings of the current study, this process is unlikely to be the origin of the complete coatings observed in the Bebertal sandstone, as none of the characteristic features, such as grain bridging menisci, preferred directions of deposition, or crinkly to flaky surfaces were observed (Worden & Morad, 2002; Ziegler, 2006). In contrast, tangential illite coatings, as shown in Fig. 6, generally follow the grain boundaries as opposed to bridging the grains. Therefore, the coating formation likely commenced with the local precipitation or deposition of thin but widespread syn-depositional smectite and hematite (Fig. 11a), as indicated by the thinner coatings in areas with early calcite cements (Fig. 4). Subsequently, these precursor smectites were illitized and compacted during burial and prevented extensive quartz cementation after burial. During the Triassic to Early Jurassic fluid flow event, these coatings likely served as important substrates for the expansive growth of the grain-covering tangential illite in open pores (Fig. 11c). The authigenic growth of these grain-covering coatings is indicated by the enclosed authigenic micro-quartz crystals (Fig. 6c), which are likely to be older than the post-illite crystallization of quartz proposed by Fischer et al. (2012). The tangential orientation of the predominantly lath- and irregular-shaped illite crystals are unusual and could well be the effect of pervasive fluid flow over tens of millions of years (Gaupp et al., 1993; Zwingmann et al., 1998). The post-growth alteration may also have then led to further thickening and amalgamation (Wilkinson et al., 2014).

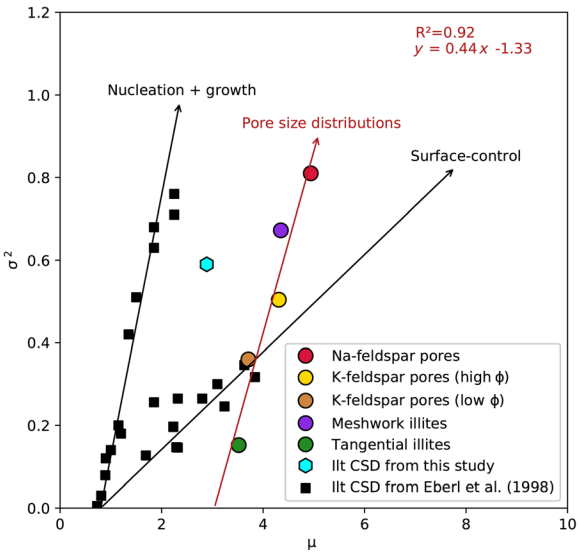

Fig. 12 Crystal-growth mechanism diagram from Eberl et al. (1998) expanded by the PSDs and the illite CSD from the present study. When plotting μ against σ^2, parameters deduced from the log-normal distribution parameters of the PSDs, a trend similar but parallel-shifted to the nucleation and growth mechanism was observed. Some data points from the original figure were excluded for visual reasons

The texturally younger pore filling-illites can be linked to the second generation of illite crystallization that has been regionally dated at 190–155 Ma (Zwingmann et al., 1998). These pore-filling lath-shaped to fibrous crystals nucleated on both tangential coatings and K-feldspar surfaces and formed coalesced sheets or open-pore fillings (Figs. 6e,f and 11d). Due to their well defined crystal shapes, the $1M_{tv}$ polytype recognized in random powder XRD patterns (Fig. 3b) likely corresponds to this second generation of illite crystals. This polytype is common to similar crystal shapes observed in a variety of sandstones characterized by K-rich pure illites where K-bearing detrital minerals acted as precursors (Meunier & Velde, 2004). In these cases, a significant amount of the K was probably derived from local, grain-scale dissolution and neocrystallization reactions.

Pore-size Distributions and Relationships to Illite Crystal Growth

The pore structures in K-feldspar grains and the illite-replacements are notably heterogeneous. The large differences between low- and high-φ K-feldspars are probably related to the porosity established during the initial stage of feldspar dissolution. In larger intragranular

pores, illites form more fibrous crystals compared to the more compacted curly illites observed in the low-φ sample. The total porosity, φ, of all analyzed textural domains varies significantly due to the occurrence of channeled structures or intergranular porosity. The PDF transformations allow a direct comparison of matrix-related pore-size parameters (Table 4). Differences between the textural domains are also revealed by the shapes of their PSDs, as expressed by the log-normal parameters of μ and σ. Increasing μ values correspond to larger mean pore radii and higher σ values to a broader range of the pore-size distributions. Importantly, these two parameters show a strong linear correlation whereby the larger the pore radii the broader the pore-size distributions (Fig. 12). Interestingly, the pore-size distributions for high-φ K-feldspar and meshwork illite show remarkably similar characteristics. This supports the idea that the meshwork textures represent intensely altered K-feldspars where the grain boundaries are no longer evident. These illite-rich areas contrast with the PSDs of: (1) the low-φ K-feldspar being dominated by pores within the K-feldspar cement; (2) the Na-feldspar containing IntraP pores; and (3) the tangential illite coatings characterized by grain-boundary pore space located at the interface with calcite crystals (Fig. 8b).

When plotted on the crystal growth mechanism diagram of Eberl et al. (1998), the linear correlation between the μ and σ^2 parameters of the different PSDs defines a trend that can be compared with the different growth mechanisms based on changes in CSDs (Fig. 12). Assuming the pore spaces are linked primarily to the growth mechanism of illite crystals, i.e. monomineralic growth within the pores and the different textural types represent a pore-filling crystal growth sequence, then this trend can be used to predict the mechanism of illite crystal growth. Based on these assumptions, continuous nucleation and growth mechanisms are indicated. That the curve is shifted towards larger mean sizes and intercepts the horizontal axis at μ = 3 (R_p = 20.1 nm) could reflect the starting pore size at the time of the initial nucleation. This is likely to represent the average pore sizes inside the unaltered K-feldspar crystals or within any substrate material that initially coated the grains (e.g. smectite or illite-smectite precursors). Plotting the log-normal parameters of the CSD determined by *MudMaster* for the total population of illites in the <1 μm size fraction, as expected, does not lie along the PSD line but is shifted toward small sizes. This reflects the smaller dimensions of the illite crystallite thicknesses (mean 24.7 nm) compared to the size of the pores between the crystals. However, assuming the CSD falls along a common trend parallel to the various PSD determinations, it indicates that illite nucleation commenced with particles ~5 nm in size (μ = 1.6, Fig. 12).

Even though two distinct phases of illite formation are recognizable in the Bebertal sandstone, the common trend in the PSDs of the different textural sites is indicative of common crystal growth mechanisms. Eberl and Velde (1989) proposed this growth mechanism may induce many stacking faults within the illite crystals as new particles nucleate on existing illite layers. This corresponds to a large amount of $1M_d$ illite as quantified by Rietveld refinements. The similar compositions of the illite in K-feldspars, the illite meshworks, and the grain coatings of illite all indicate similar amounts of interlayer cations that correspond to ~5% of intercalated smectite layers within the $1M_d$ illite. The grain coatings also include well-developed sheets containing randomly oriented laths, which according to Güven (2001) nucleate on substrates showing a high degree of disorder. Other areas of these grain coatings also contain intergrown lath crystals at 60° and 120° of the $1M_{tv}$ polytype similar to those described by Pevear (1999), Schleicher et al. (2006), and Laverret et al. (2006). The agglomeration of diverse crystal shapes is also similar to those observed by Lanson and Champion (1991), which were attributed to the post-growth alteration of lath-shaped illites transforming into hexagonal crystals. Although the analysis of different textural types of illite did not cover the fibrous pore-filling illites, which were not possible to study due to their delicate structures, the common trend of PSDs for all the textural pore types studied do indicate the younger stage of lath-shaped illite growth, which contributed to grain coatings and pore-fillings, also formed by continuous nucleation and growth from circulating fluids during the Jurassic.

As the PSD values for the primary pores of albite fall along the same crystal growth trend as those observed for the illite pores (Fig. 12), this approach may be applicable to other diagenetic minerals. For example, Worden and Rushton (1992) described similar diagenetic feldspar overgrowths with small primary pores, which were also considered to have formed by continuous nucleation and growth. However, note that the single PSD value for diagenetic albite of the Bebertal sandstone is currently insufficient to establish a reliable PSD trend and more data is required to verify this interpretation.

Porosity and Permeability Characteristics and Relationships to Reservoir Properties

In terms of permeability, the modeled nanoscale transport properties in this study are 3 to 4 orders of magnitude smaller than those obtained from CT-scale simulations and direct measurements (Heidsiek et al., 2020; Jacob et al., 2021). This indicates that the nanoporous systems are, at the plug scale, widely detached from the effective transport pathways measured under laboratory conditions. However, under the lithostatic pressures of the subsurface environment, significantly lower, plug-scale permeabilities can be expected due to compression of the pore systems and enhanced pore pressures. Nanoporous illite structures are, therefore, considered to become more relevant once pore pressures exceed the capillary entry pressures of these structures (Busch & Amann-Hildenbrand, 2013) or as tight reservoir sandstones lose more permeability as a consequence of further crystal growth or particle mobilization in the diagenetic environment.

The permeabilities of the analyzed nano-porous structures range from 13.4 to 1.4 μd and their growth significantly altered flow paths over time (Fig. 11). The generation of nano-porous systems commenced with the second generation of K-feldspar cementation, which formed permeable and connected-channel pore networks within the nanocrystalline cement matrix. This led to a reduction of porosity and permeability, both of which reached its lowest level after the Late Permian dissolution event. The subsequent formation of widespread tangential grain coatings, which do not exhibit perpendicular pore paths, further lowered the porosity and permeability by the reduction of intergranular pore-throat sizes and by sealing intragranular pore networks. Although the formation of K-feldspar replacing illite meshworks generated intergranular permeable porosity, the expansive nature of these structures into the open pore space negatively affected the overall rock permeability.

As the older generations of illite formed more stable, coalesced layers up to 2 μm thick, the younger generation of pore-filling illite laths and fibers are the phases that represent the more fragile structures within this sandstone. These crystals appear in places only weakly attached to substrate surfaces and commonly project out into the open pore space. Because these illites are of $1M_{tv}$ polytype, quantification of the bulk polytype composition, and their crystal shapes and sizes, provide important information for predicting any future mobilization of them. Such mobilization is relevant when new fluids are injected into these reservoir rocks for future gas-storage purposes.

Conclusions

1. Detailed 3D pore-space analyses by FIB-SEM combined with modeling of the fluid flow through the different textural sub-domains of a tight reservoir sandstone provide a powerful tool for reconstructing diagenetic history and for predicting in more detail microstructurally dependent petrophysical properties.
2. Two distinct events of illite crystallization were distinguished that have characteristic textural and petrophysical properties such as porosity and permeability. The older generation of illites of probable Early Jurassic age formed locally: illites in K-feldspar grains; more extensively altered meshwork structures; and thin but widespread grain coatings. These structures were formed by crystals of the $1M_d$ polytype. A younger generation of illites of probable Late Jurassic age formed overgrowths comprising delicate pore-filling lath-shaped and fibrous varieties of the $1M_{tv}$ polytype.
3. The nanoporous structure of the various illite reaction textures indicate a genetic relationship between their pore-size distribution and a common crystal-growth mechanism. A comparison with models based on crystallite-size distributions indicated that the main mechanism was dominated by continuous nucleation and crystal growth. The linear relationship between mean pore radii and the width of the pore-size distributions may be of interest for future modeling and upscaling approaches of reactive transport processes. The results further indicated that the observed trend may apply to a wider range of authigenic minerals, which needs to be confirmed in future studies.

Acknowledgments The authors are grateful to David Awwiller and David Quirt for their constructive feedback which helped to

improve the manuscript. This work was supported by the German Federal Ministry of Education and Research (BMBF) "Geological Research for Sustainability (GEO:N)" program of the BMBF "Research for Sustainable Development (FONA3)" activities. It is part of the project ResKin (Reaction kinetics in reservoir rocks, 03G0871B). The authors also thank Cornelius Fischer for his feedback on an earlier version of this manuscript and the continuous support of the ResKin team. This study used DFG-funded XRD, FIB-SEM, and TEM instrumentation (project numbers 108031954, 173095180, and 428027021).

Author Contribution Conceptualization: Markus Peltz, Laurence N. Warr; Formal analysis: Markus Peltz, Arne Jacob; Investigation: Markus Peltz, Arne Jacob; Methodology: Markus Peltz; Project administration: Laurence N. Warr, Michael Kersten; Software: Markus Peltz, Arne Jacob; Supervision: Michael Kersten, Laurence N. Warr; Validation: Georg H. Grathoff, Frieder Enzmann, Michael Kersten, Laurence N. Warr; Visualization: Markus Peltz; Writing – original draft: Markus Peltz; Writing – review & editing: Arne Jacob, Georg H. Grathoff, Frieder Enzmann, Michael Kersten, Laurence N. Warr

Funding Open Access funding enabled and organized by Projekt DEAL.

Funding sources are as stated in the Acknowledgments.

Data Availability FIB-SEM datasets are available upon reasonable request.

Declarations

Consent to Participate Not applicable.

Consent for Publication Not applicable.

Conflict of Interest The authors declare that they have no conflict of interest.

References

Aldega, L., & Eberl, D. D. (2005). Detrital illite crystals identified from crystallite thickness measurements in siliciclastic sediments. *American Mineralogist, 90*(10), 1587–1596. https://doi.org/10.2138/am.2005.1823

Bauer, A., Velde, B., & Gaupp, R. (2000). Experimental constraints on illite crystal morphology. *Clay Minerals, 35*(3), 587–597. https://doi.org/10.1180/000985500546909

Berg, S., Kutra, D., Kroeger, T., Straehle, C. N., Kausler, B. X., Haubold, C., Schiegg, M., Ales, J., Beier, T., Rudy, M., Eren, K., Cervantes, J. I., Xu, B., Beuttenmueller, F., Wolny, A., Zhang, C., Koethe, U., Hamprecht, F. A., & Kreshuk, A. (2019). Ilastik: Interactive machine learning for (bio)image analysis. *Nature Methods, 16*(12), 1226–1232. https://doi.org/10.1038/s41592-019-0582-9

Berg, S., Saxena, N., Shaik, M., & Pradhan, C. (2018). Generation of ground truth images to validate micro-CT image-processing pipelines. *The Leading Edge, 37*(6), 412–420. https://doi.org/10.1190/tle37060412.1

Bergmann, J., Friedel, P., & Kleeberg, R. (1998). BGMN – a new fundamental parameters based Rietveld program for laboratory X-ray sources, its use in quantitative analysis and structure investigations. *CPD Newsletter*, (20), 5–8.

Bjørlykke, K. (2014). Relationships between depositional environments, burial history and rock properties. Some principal aspects of diagenetic process in sedimentary basins. *Sedimentary Geology, 301*, 1–14. https://doi.org/10.1016/j.sedgeo.2013.12.002

Busch, A., & Amann-Hildenbrand, A. (2013). Predicting capillarity of mudrocks. *Marine and Petroleum Geology, 45*, 208–223. https://doi.org/10.1016/j.marpetgeo.2013.05.005

Darby, D., Wilkinson, M., Fallick, A. E., & Haszeldine, R. S. (1997). Illite dates record deep fluid movements in petroleum basins. *Petroleum Geoscience, 3*(2), 133–140. https://doi.org/10.1144/petgeo.3.2.133

Desbois, G., Urai, J. L., Hemes, S., Schröppel, B., Schwarz, J.-O., Mac, M., & Weiel, D. (2016). Multi-scale analysis of porosity in diagenetically altered reservoir sandstone from the Permian Rotliegend (Germany). *Journal of Petroleum Science and Engineering, 140*, 128–148. https://doi.org/10.1016/j.petrol.2016.01.019

Doebelin, N., & Kleeberg, R. (2015). Profex: A graphical user interface for the Rietveld refinement program BGMN. *Journal of Applied Crystallography, 48*(Pt 5), 1573–1580. https://doi.org/10.1107/S1600576715014685

Eberl, D. D., & Velde, B. (1989). Beyond the Kübler index. *Clay Minerals, 24*(4), 571–577. https://doi.org/10.1180/claymin.1989.024.4.01

Eberl, D. D., Drits, V. A., & Srodon, J. (1998). Deducing growth mechanisms for minerals from the shapes of crystal size distributions. *American Journal of Science, 298*(6), 499–533. https://doi.org/10.2475/ajs.298.6.499

Eberl, D. D., Drits, V. A., Srodon, J., & Nüesch, R. (1996). *MUDMASTER: A Program for Calculating Crystalline Size Distributions and Strain from the Shapes of X-Ray Diffraction Peaks* (Open-File Report). US Geological Survey.

Fischer, C., Dunkl, I., von Eynatten, H., Wijbrans, J. R., & Gaupp, R. (2007). A 3D high resolution model of bounding surfaces in aeolian-fluvial deposits: An outcrop analogue study from the Permian Rotliegend, Northern Germany. *Journal of Petroleum Geology, 30*(3), 257–273. https://doi.org/10.1111/j.1747-5457.2007.00257.x

Fischer, C., Dunkl, I., von Eynatten, H., Wijbrans, J. R., & Gaupp, R. (2012). Products and timing of diagenetic processes in Upper Rotliegend sandstones from Bebertal (North German Basin, Parchim Formation, Flechtingen High, Germany). *Geological Magazine, 149*(5), 827–840. https://doi.org/10.1017/S0016756811001087

Gaupp, R., & Okkerman, J. A. (2011). Diagenesis and reservoir quality of Rotliegend sandstones in the northern Netherlands—a review. In J. Grötsch (Ed.), *SEPM special publication: Vol. 98. The Permian Rotliegend of the Netherlands* (Vol. 98). Society for Sedimentary Geology.

Gaupp, R., Matter, A., Platt, J. D., Ramseyer, K., & Walzebuck, J. (1993). Diagenesis and fluid evolution of deeply buried Permian (Rotliegende) gas reservoirs, Northwest Germany. *AAPG Bulletin*, *77*. https://doi.org/10.1306/BDFF8E0C-1718-11D7-8645000102C1865D

Gharrabi, M. (1998). The transformation of illite to muscovite in pelitic rocks: Constraints from X-ray diffraction. *Clays and Clay Minerals, 46*(1), 79–88. https://doi.org/10.1346/CCMN.1998.0460109

Glennie, K. W., Mudd, G. C., & Nagtegaal, P. J. C. (1978). Depositional environment and diagenesis of Permian Rotliegendes sandstones in Leman Bank and Sole Pit areas of the UK southern North Sea. *Journal of the Geological Society, 135*(1), 25–34. https://doi.org/10.1144/gsjgs.135.1.0025

Grathoff, G. H., & Moore, D. M. (1996). Illite polytype quantification using Wildfire© calculated X-ray diffraction patterns. *Clays and Clay Minerals, 44*(6), 835–842. https://doi.org/10.1346/CCMN.1996.0440615

Griffiths, J., Worden, R. H., Wooldridge, L. J., Utley, J. E. P., & Duller, R. A. (2018). Detrital clay coats, clay minerals, and pyrite: A modern shallow-core analogue for ancient and deeply buried estuarine sandstones. *SEPM Journal of Sedimentary Research, 88*(10), 1205–1237. https://doi.org/10.2110/jsr.2018.56

Güven, N. (2001). Mica structure and fibrous growth of illite. *Clays and Clay Minerals, 49*(3), 189–196. https://doi.org/10.1346/CCMN.2001.0490301

Hancock, N. J. (1978). Possible causes of Rotliegend sandstone diagenesis in northern West Germany. *Journal of the Geological Society, 135*(1), 35–40. https://doi.org/10.1144/gsjgs.135.1.0035

Heidsiek, M., Butscher, C., Blum, P., & Fischer, C. (2020). Small-scale diagenetic facies heterogeneity controls porosity and permeability pattern in reservoir sandstones. *Environmental Earth Sciences, 79*(18). https://doi.org/10.1007/s12665-020-09168-z

Jacob, A., Peltz, M., Hale, S., Enzmann, F., Moravcova, O., Warr, L. N., Grathoff, G., Blum, P., & Kersten, M. (2021). Simulating permeability reduction by clay mineral nanopores in a tight sandstone by combining computer X-ray microtomography and focussed ion beam scanning electron microscopy imaging. *Solid Earth, 12*(1), 1–14. https://doi.org/10.5194/se-12-1-2021

Lander, R. H., & Bonnell, L. M. (2010). A model for fibrous illite nucleation and growth in sandstones. *AAPG Bulletin, 94*(8), 1161–1187. https://doi.org/10.1306/04211009121

Lanson, B., & Champion, D. (1991). The I/S-to-illite reaction in the late stage diagenesis. *American Journal of Science, 291*(5), 473–506. https://doi.org/10.2475/ajs.291.5.473

Lanson, B., Beaufort, D., Berger, G., Bauer, A., Cassagnabère, A., & Meunier, A. (2002). Authigenic kaolin and illitic minerals during burial diagenesis of sandstones: A review. *Clay Minerals, 37*(1), 1–22. https://doi.org/10.1180/0009855023710014

Laverret, E., Mas, P. P., Beaufort, D., Kister, P., Quirt, D., Bruneton, P., & Clauer, N. (2006). Mineralogy and geochemistry of the host-rock alterations associated with the shea creek unconformity-type uranium deposits (Athabasca Basin, Saskatchewan, Canada). Part 1. Spatial variation of illite properties. *Clays and Clay Minerals, 54*(3), 275–294. https://doi.org/10.1346/CCMN.2006.0540301

Loucks, R. G., Reed, R. M., Ruppel, S. C., & Hammes, U. (2012). Spectrum of pore types and networks in mudrocks and a descriptive classification for matrix-related mudrock pores. *AAPG Bulletin, 96*(6), 1071–1098. https://doi.org/10.1306/08171111061

Mehra, O. P., & Jackson, M. L. (1960). Iron oxide removal from soils and clays by a dithionite-citrate system buffered with sodium bicarbonate. In A. Swineford (Ed.), *Clays and clay minerals: proceedings of the seventh national conference on clays and clay minerals* (pp. 317–327). Elsevier Science. https://doi.org/10.1016/B978-0-08-009235-5.50026-7

Menning, M., Gast, R., Hagdorn, H., Käding, K.-C., Simon, T., Szurlies, M., & Nitsch, E. (2006). Zeitskala fur Perm und Trias in der stratigraphischen Tabelle von Deutschland 2002, zyklostratigraphische Kalibrierung der Hoheren Dyas und Germanischen Trias und das Alter der Stufen Roadium bis Rhaetium 2005. *Newsletters on Stratigraphy, 41*(1-3), 173–210. https://doi.org/10.1127/0078-0421/2005/0041-0173

Merriman, R. J., & Kemp, S. J. (1996). Clay minerals and sedimentary basin maturity. *Mineralogical Society Bulletin*, (111), 7–8. https://doi.org/10.1127/0935-1221/2005/0017-0007

Meunier, A., & Velde, B. (2004). *Illite: Origins, Evolution and Metamorphism*. Springer. https://doi.org/10.1007/978-3-662-07850-1

Moore, D. M., & Reynolds, R. C. (1997). *X-ray diffraction and the identification and analysis of clay minerals* (2nd ed.). Oxford University Press.

Morad, S., Al-Ramadan, K., Ketzer, J. M., & de Ros, L. F. (2010). The impact of diagenesis on the heterogeneity of sandstone reservoirs: A review of the role of depositional facies and sequence stratigraphy. *AAPG Bulletin, 94*(8), 1267–1309. https://doi.org/10.1306/04211009178

Münch, B., & Holzer, L. (2008). Contradicting geometrical concepts in pore size analysis attained with electron microscopy and mercury intrusion. *Journal of the American Ceramic Society, 91*(12), 4059–4067. https://doi.org/10.1111/J.1551-2916.2008.02736.X

Pedrosa, E. T., Fischer, C., Morales, L. F., Rohlfs, R. D., & Luttge, A. (2021). Influence of chemical zoning on sandstone calcite cement dissolution: The case of manganese and iron. *Chemical Geology, 559*, 119952. https://doi.org/10.1016/j.chemgeo.2020.119952

Pevear, D. R. (1999). Illite and hydrocarbon exploration. *Proceedings of the National Academy of Sciences of the United States of America, 96*(7), 3440–3446. https://doi.org/10.1073/pnas.96.7.3440

Schleicher, A. M., Warr, L. N., Kober, B., Laverret, E., & Clauer, N. (2006). Episodic mineralization of hydrothermal illite in the Soultz-sous-Forêts granite (Upper Rhine Graben, France). *Contributions to Mineralogy and Petrology, 152*(3), 349–364. https://doi.org/10.1007/s00410-006-0110-7

Seemann, U. (1982). Depositional facies, diagenetic clay minerals and reservoir quality of Rotliegend sediments in the Southern Permian Basin (North Sea): A review. *Clay Minerals, 17*(1), 55–67. https://doi.org/10.1180/claymin.1982.017.1.06

Small, J. S., Hamilton, D. L., & Habesch, S. (1992). Experimental simulation of clay precipitation within reservoir sandstones; 2, mechanism of illite formation and controls on morphology. *SEPM Journal of Sedimentary Research, 62*(3), 520–529. https://doi.org/10.2110/jsr.62.520

Środoń, J., & Eberl, D. D. (2018). 12. Illite. In S. Bailey (Ed.), *Reviews in Mineralogy & Geochemistry: Vol. 13. Micas* (pp. 495–544). De Gruyter. https://doi.org/10.1515/9781501508820-016

Storvoll, V., Bjørlykke, K., Karlsen, D., & Saigal, G. (2002). Porosity preservation in reservoir sandstones due to grain-coating illite: A study of the Jurassic Garn Formation from the Kristin and Lavrans fields, offshore mid-Norway. *Marine and Petroleum Geology, 19*(6), 767–781. https://doi.org/10.1016/S0264-8172(02)00035-1

Tang, L., Gluyas, J., & Jones, S. (2018). Porosity preservation due to grain coating illite/smectite: Evidence from Buchan Formation (Upper Devonian) of the Ardmore field, UK North Sea. *Proceedings of the Geologists' Association, 129*(2), 202–214. https://doi.org/10.1016/j.pgeola.2018.03.001

Ufer, K., Kleeberg, R., Bergmann, J., & Dohrmann, R. (2012). Rietveld refinement of disordered illite-smectite mixed-layer structures by a recursive algorithm. I: One-dimensional patterns. *Clays and Clay Minerals, 60*(5), 507–534. https://doi.org/10.1346/CCMN.2012.0600507

Warr, L. N. (2020). Recommended abbreviations for the names of clay minerals and associated phases. *Clay Minerals, 55*(3), 261–264. https://doi.org/10.1180/clm.2020.30

Weibel, R., Nielsen, M. T., Therkelsen, J., Jakobsen, F. C., Bjerager, M., Mørk, F., Mathiesen, A., Hovikoski, J., Pedersen, S. S., Johannessen, P. N., & Dybkjær, K. (2020). Illite distribution and morphology explaining basinal variations in reservoir properties of Upper Jurassic sandstones, Danish North Sea. *Marine and Petroleum Geology, 116*, 104290. https://doi.org/10.1016/j.marpetgeo.2020.104290

Weibel, R., Olivarius, M., Jakobsen, F. C., Whitehouse, M., Larsen, M., Midtgaard, H., & Nielsen, K. (2019). Thermogenetic degradation of early zeolite cement: An important process for generating anomalously high porosity and permeability in deeply buried sandstone reservoirs? *Marine and Petroleum Geology, 103*, 620–645. https://doi.org/10.1016/j.marpetgeo.2019.02.006

Wilkinson, M., Haszeldine, R. S., & Fallick, A. E. (2014). Authigenic illite within Northern and Central North Sea oilfield sandstones: Evidence for post-growth alteration. *Clay Minerals, 49*(2), 229–246. https://doi.org/10.1180/claymin.2014.049.2.06

Wilson, M. D. (1992). Inherited grain-rimming clays in sandstones from eolian and shelf environments: Their origin and control on reservoir properties. In D. W. Houseknecht & E. D. Pittman (Eds.), *Origin, diagenesis, and petrophysics of clay minerals in sandstones* (pp. 209–225). SEPM (Society for Sedimentary Geology). https://doi.org/10.2110/pec.92.47.0209

Wilson, M. D., & Pittman, E. D. (1977). Authigenic clays in sandstones: Recognition and influence on reservoir properties and paleoenvironmental analysis. *SEPM Journal of Sedimentary Research, 47*. https://doi.org/10.1306/212F70E5-2B24-11D7-8648000102C1865D

Worden, R. H., & Morad, S. (Eds.). (2002). *Special publication number 34 of the International Association of Sedimentologists. Clay mineral cements in sandstones*. Blackwell Pub. https://doi.org/10.1002/9781444304336

Worden, R. H., & Rushton, J. C. (1992). Diagenetic K-feldspar textures: A TEM study and model for diagenetic feldspar growth. *SEPM Journal of Sedimentary Research, Vol., 62*. https://doi.org/10.1306/D42679D8-2B26-11D7-8648000102C1865D

Yuan, G., Cao, Y., Schulz, H.-M., Hao, F., Gluyas, J., Liu, K., Yang, T., Wang, Y., Xi, K., & Li, F. (2019). A review of feldspar alteration and its geological significance in sedimentary basins: From shallow aquifers to deep hydrocarbon reservoirs. *Earth-Science Reviews, 191*, 114–140. https://doi.org/10.1016/j.earscirev.2019.02.004

Ziegler, K. (2006). Clay minerals of the Permian Rotliegend Group in the North Sea and adjacent areas. *Clay Minerals, 41*(1), 355–393. https://doi.org/10.1180/0009855064110200

Zwingmann, H., Clauer, N., & Gaupp, R. (1998). Timing of fluid flow in a sandstone reservoir of the North German Rotliegend (Permian) by K-Ar dating of related hydrothermal illite. *Geological Society, London, Special Publications, 144*(1), 91–106. https://doi.org/10.1144/GSL.SP.1998.144.01.07

Zydney, A. L., Aimar, P., Meireles, M., Pimbley, J. M., & Belfort, G. (1994). Use of the log-normal probability density function to analyze membrane pore size distributions: Functional forms and discrepancies. *Journal of Membrane Science, 91*(3), 293–298. https://doi.org/10.1016/0376-7388(94)80090-1